On the Combination of Dual-Polarization Sentinel-1 Ascending/Descending Orbiting Passes to Estimate Damage Due to the 2016 Central Italy Earthquake

Emanuele Ferrentino, *Student Member, IEEE*, Ferdinando Nunziata, *Senior Member, IEEE*, Christian Bignami, *Member, IEEE*, Laura Graziani, Alessandra Maramai, Maurizio Migliaccio, *Fellow, IEEE*, and Salvatore Stramondo, *Senior Member, IEEE*

***Abstract*—This study investigates the extra benefit provided by the joint use of synthetic aperture radar (SAR) polarimetric diversity and ascending/descending orbit passes to quantify postearthquake damage that occurred over the area of Amatrice, an Italian city significantly damaged by the 2016 Central Italy earthquake. First, the sensitivity of PolSAR features derived from SAR scenes collected under ascending/descending orbits to the damage is investigated. Then, the damage assessment is performed using a processing chain that consists of extracting dual-polarimetric SAR features to detect damage and, then, applying a fuzzy clustering scheme, to partition the feature outputs into damage levels. This processing chain is first separately applied to Sentinel-1 SAR scenes collected under ascending/descending orbits; then the processing outputs are merged using two different approaches. To discuss the quality of the estimated damage maps, ground information collected by surveys performed by a trained team is used. Experimental results show that the joint use of ascending/descending orbit passes improves the estimation of damage levels (up to 78%) with respect to the estimation performed using the orbiting passes separately.**

***Index Terms*—Change detection, classification, earthquake, PolSAR.**

I. Introduction

SATELLITE remote sensing plays an important role to observe changes induced by earthquakes. During a seismic event, fast and noncooperative assessment of damage is a vital step to postdisaster emergency response and to reduce the impact of the disaster, while helping postdisaster reconstruction activities [1], [2]. Within this context, remotely sensed imagery are of paramount importance due to their synoptic and noncooperative capabilities. Among the remote sensing instruments, optical sensors are very often used [1]. However, optical radiation is severely affected by cloud cover, solar illumination, and other adverse meteorological conditions that limit its operational use. In contrast, radar sensors ensure all-day and almost all-weather observations, together with a wide area coverage. In particular, the synthetic aperture radar (SAR), due to its fine spatial resolution imaging capabilities, can be very useful to observe damage caused by earthquakes [1]. SAR methods are mainly based on single-polarization (SP) measurements and consist of exploiting the information and features derived from interferometric coherence and/or the normalized radar cross section (NRCS) measured on image pairs collected before and after the earthquake [3], [4]. In [3] and [5], the 1995 Hyogoken–Nanbu (Kobe) earthquake is analyzed using C-band European Remote-Sensing satellite ERS-1 SAR imagery collected before and after the earthquake. Experimental results show that within the damaged areas, identified using ground survey data collected after the earthquake, both the coherence and the backscattering intensity decrease. In [6], an approach based on the joint exploitation of pixel-based and feature-based information is proposed to detect damaged areas. Experiments performed using Environmental Satellite (ENVISAT) Advanced SAR (ASAR) imagery collected over the city of Bam, Iran, during the earthquake occurred in 2003, show that the joint use of the two sources of information provides the best performance.

To improve the performance of SAR-based methods in observing earthquake damaged areas, SAR measurements are often augmented with optical data [1], [2], [7], [8]. The 2009 Central Italy earthquake is analyzed in [9] using very high resolution (VHR) TerraSAR-X HH-polarized SAR imagery and optical measurements acquired by QuickBird. The damage analysis, performed on a building basis, points out the benefits of SAR-observations to classify buildings calling for different damage levels. In [1], the joint use of SAR and optical measurements collected by Indian Remote Sensing (IRS)1-C and the Advanced Spaceborne Thermal Emission and Reflection Radiometer (ASTER), are exploited to evaluate urbanized areas damaged by the earthquakes occurred in 1999 and 2003 over the cities of Izmit, Turkey, and Bam, Iran, respectively. Experimental results show that the joint combination of SAR and optical measurements allow detecting three classes of damaged areas with an accuracy around 90%. In [2], a machine-learning classifier is developed to identify buildings damaged by the earthquake occurred in 2008 in Wenchuan, China. Experimental results,

Manuscript received 3 August 2022; revised 25 October 2022; accepted 25 October 2022. Date of publication 28 October 2022; date of current version 10 November 2022. *(Corresponding author: Emanuele Ferrentino.)*

Emanuele Ferrentino and Maurizio Migliaccio are with the Dipartimento di Ingegneria, Università degli Studi di Napoli Parthenope, 80133 Napoli, Italy, and also with the Istituto Nazionale di Geofisica e Vulcanologia, 00143 Rome, Italy (e-mail: emanuele.ferrentino@ingv.it; mnm.migliaccio@gmail.com).

Ferdinando Nunziata, Christian Bignami, Laura Graziani, Alessandra Maramai, and Salvatore Stramondo are with the Dipartimento di Ingegneria, Università degli Studi di Napoli Parthenope, 80133 Napoli, Italy (e-mail: ferdinando.nunziata@uniparthenope.it; christian.bignami@ingv.it; laura.graziani@ingv.it; alessandra.maramai@ingv.it; salvatore.stramondo@ingv.it).

Digital Object Identifier 10.1109/JSTARS.2022.3217889

undertaken using very high resolution (VHR) postearthquake TerraSAR-X Staring Spotlight Imagery and original building footprint maps obtained from a combination of postearthquake Laser Imaging Detection and Ranging (LIDAR) data and in situ observation, show that the method can distinguish between collapsed and standing buildings, with an overall accuracy of approximately 90%. In [7], X-band TerraSAR-X SAR imagery and optical measurements collected by GeoEye-1 are jointly used to observe damage related to the earthquake occurred in Haiti in 2010. Two operational classifiers and ground-based information are used to discuss the accuracy of the damage maps. Experimental results show that a 66% accuracy is achieved when the classifiers are applied at city block scale and considering three damage levels.

Nowadays, the increasing number of spaceborne missions equipped with multipolarization SAR triggered new added-value products in the urban domain. Within this context, several studies have been proposed to exploit full-polarimetric (FP) SAR measurements to detect damage due to earthquake [10], [11]. However, the operational use of FP SAR is still limited to experimental campaigns; while simpler polarimetric configurations, e.g.; the dual-polarimetric (DP) SAR [12], [13], are often preferred as standard imaging mode, such as in the case of the Copernicus Sentinel-1 mission that routinely collect DP SAR imagery. Only a few studies have been proposed to exploit DP SAR measurements to observe urbanized areas damaged by earthquakes [14], [15], [16], [17], [18], which demonstrate that the extra information provided by polarization diversity results in more accurate estimations of damaged areas. In [14], the 2015 Gorkha (Nepal) earthquake is addressed using DP ALOS-PALSAR 2 L-band SAR imagery and a metric based on the interferometric coherence is applied to both co- and cross-polarized channels to detect damaged buildings. The cross-polarized channel is found to achieve an accuracy around 35.1%. In [15], collapsed buildings are identified using DP ALOS-PALSAR 2 L- and Sentinel-1 C-band SAR imagery. By using both intensity and coherence features, the cross-polarized channel allowed to identify collapsed building with an accuracy around 84%. In [16] and [18], the sensitivity of the interchannel coherence to earthquake-induced damage is investigated using DP SAR imagery collected by Sentinel-1 over the 2016 Central Italy earthquake. Experimental results demonstrate that DP information improves the detection of the damaged area with respect to single polarization SAR imagery. In addition, DP features enable to the use of just a pair of SAR scenes (collected before and after the event) to implement the change detection approach. It must be explicitly pointed out that a fair comparison among the accuracy of the SAR-based damage maps estimated by state-of-the-art methods is not straightforward since typically each method calls for a specific level of building aggregation. Most of the methods deal with a damage analysis at city block level, i.e., the damage level refers to an aggregated of buildings [7]. Other methods, in particular the ones developed for VHR SAR imagery, can provides damage analysis at building scale [2].

The observation of built-up areas through side-looking radars is significantly affected by the geometry of the imaging system with imagery collected under ascending and descending orbits providing typically different information [19]. This means that, at least in principle, it is worth expecting that joint use of the two passes may contribute to a better observation of built-up areas since details that appear in a given pass may not observable (or they can appear distorted) in the opposite pass. In the context of earthquake damage assessment, only few studies addressed the joint use of ascending/descending passes. In [17], the 2016 Central Italy Earthquake is analyzed using Sentinel-1 DP dataset collected in both ascending and descending passes. Results pointed out that imagery collected under ascending and descending passes carry on complementary information. In [20], ascending and descending COSMO-SkyMed HH-polarized imagery are properly combined to enhance the detection of collapsed building. The ascending and descending datasets are integrated using two models based on discriminant analysis and fuzzy logic. Results confirm that the combination of ascending/descending passes improve the detection performance.

This study explores the extra-benefit arising from the joint use of polarimetric diversity and ascending/descending orbiting passes to improve the estimation of damage levels in earthquake-affected urbanized areas. The polarimetric information is used to design robust and effective change detection approaches; while ascending and descending orbiting passes are exploited to enrich the level of information related to the observed scene. The processing scheme is designed as follows: 1) dual polarimetric change detection features [16], [17] are used to detect the changes that occurred after the earthquake; 2) an unsupervised classifier based on Fuzzy c-means clustering is adopted to associate changes in a proper class of damage; 3) the ascending and descending damage maps are properly combined and contrasted with the ground truth obtained by in situ measurements.

Experimental results, obtained processing a set of DP Sentinel-1 SAR imagery collected over the Central Italy area affected by the 2016 Earthquake, show that the joint use of ascending and descending datasets processed using the DP approach improves the estimation performance reaching an overall accuracy up to 78%.

II. Test Site and Dataset

On 24 August 2016, at 01:36 Greenwich Mean Time (GMT), a moment magnitude scale Mw 6.0 earthquake struck a large portion of the central Apennines fold and thrust belt, between the towns of Norcia and Amatrice. The main event was followed by a second earthquake (Mw 5.4) about 1 h later. This seismic sequence caused the death of nearly 300 people and widespread destruction of entire villages. The epicenters were located from the Istituto Nazionale di Geofisica e Vulcanologia (INGV) close to the city of Accumoli in the Rieti province, where the area mostly affected by the earthquake extended for about 40 km along with the North West-South East (NW-SE) direction. Most of the collapsed buildings are located in the older western part of the city of Amatrice, see the correspondent Google Earth image shown in Fig. 1(a), where the ground information on the levels of damage, which consists of 472 samples, is also

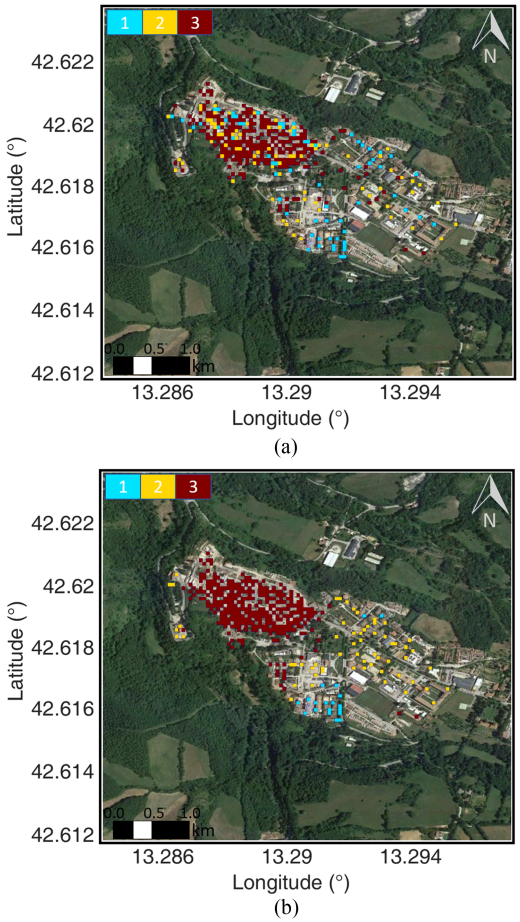

Fig. 1. Google Earth image related to the older western part of the city of Amatrice: (a) the pixels correspond to the ground truth obtained by in-situ measurements, where each color is related to a degree of damage; (b) the same pixels are smoothed using a 15×15 average moving window.

TABLE I
SENTINEL–1 SAR DATASET

Acquisition date	Resolution (range× azimuth) (m)	Acquisition mode	Polarization	Angle of incidence
22 August, 2016	2.33 × 13.92	Ascending	DP (VV+VH)	≈ 34°
3 September, 2016	2.33 × 13.92	Ascending	DP (VV+VH)	≈ 34°
21 August, 2016	2.33 × 13.92	Descending	DP (VV+VH)	≈ 41°
2 September, 2016	2.33 × 13.92	Descending	DP (VV+VH)	≈ 41°

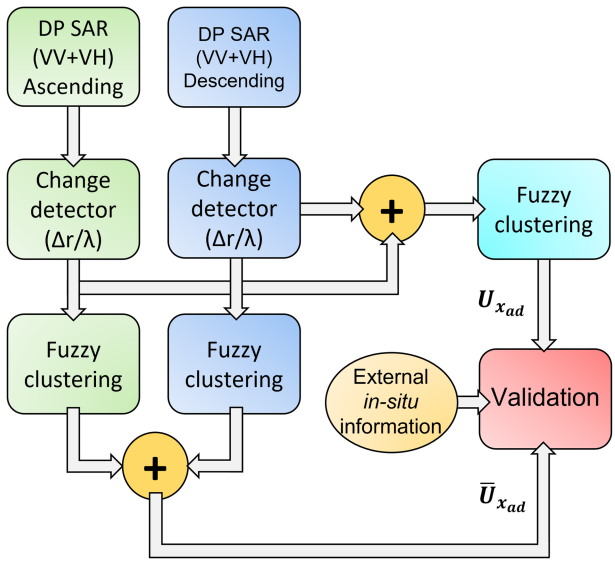

Fig. 2. Block diagram of the proposed approach where $U_{x_{ad}}$ and $\bar{U}_{x_{ad}}$ stands for output obtained combining PolSAR features (λ, r) related to ascending and descending orbits (a, d) before and after the fuzzy clustering, respectively. To validate the accuracy of the estimated damage levels, external ground information is used.

annotated. This ground information is provided by the INGV Quick Earthquake Survey team (QUEST) and comes from a macroseismic survey performed immediately after the event on the damaged area [21], [22]. The QUEST performed a field campaign, where different municipality areas (or part of them) were simultaneously inspected to estimate their macroseismic intensity value according to the European Macroseismic Scale (EMS98) [23]. The latter, which focuses on the damage affecting residential building stocks, classifies buildings into six classes of vulnerability and distinguishes five damage classes (from negligible damage up to the destruction of the building). During the field survey, each building was labeled according to the vulnerability and the degree of damage. As previously discussed in [18] light levels of damage can be hardly recognized in SAR imagery. Hence, to allow a fairer intercomparison between ground information and SAR-derived damage, the granularity of ground information is reduced. Damage that, according to the EMS98 scale, belong to classes 1 and 2 (i.e., light damage) is merged into a single class. Damage that correspond to classes 4 and 5 (i.e., heavily and completely destroyed buildings) is grouped into a single class. This implies that the granularity of the ground information is reduced to the classes that are depicted in Fig. 1(a). In addition, the ground truth data, which is intrinsically a point-wise measure, was smoothed to be more compliant with SAR resolution and the derived features obtained by averaging pixels with a predefined moving window. The smoothed ground truth, using a $N \times N$ average moving window, with $N = 15$, is shown in Fig. 1(b).

The satellite dataset consists of four single look complex (SLC) DP polarized SAR imagery collected before and after the earthquake by the Copernicus Sentinel-1 mission over the area of Amatrice (Lazio, Italy) in ascending and descending orbits, with an incidence angle of around 34° and 41°, respectively (see Table I).

III. PROPOSED METHODOLOGY

In this section, the methodology adopted to generate damage maps from the fusion of multipolarization SAR imagery acquired in ascending and descending orbit is described (see Fig. 2).

The first step is to preprocess the SAR dataset by: 1) coregistrating separately ascending and descending imagery; 2) performing radiometric calibration and; 3) speckle-filtering SAR imagery with a 5×5 pixel boxcar filter. The second step is

to apply polarimetric change detection methods on a pair of DP SAR imagery collected before and after the earthquake. Then, the change detection features extracted from ascending and descending dataset are geocoded. The third step is to quantify damage levels by jointly exploiting the output of the multipolarization features and ascending/descending orbits using an unsupervised fuzzy clustering image segmentation approach.

A. Change Detection Using DP SAR Features

In this section, DP change detection approaches developed in [16] and [17] to detect changes occurred after an earthquake in the scene collected under ascending and descending orbits are briefly described.

The observation of damage induced by the earthquake in the urbanized areas is performed using two DP metrics. The first metric exploits the reflection symmetry [16], [24], [25]; i.e., a property that is always satisfied by natural distributed scenario; while it is not satisfied by man-made targets. Under the assumption of reflection symmetry, the coherence between co- and cross-polarized channels vanishes [25]

$$\langle S_{VV} S_{VH}^{*} \rangle = \langle S_{HH} S_{HV}^{*} \rangle = 0. \tag{1}$$

Following this theoretical rationale, a metric, based on the amplitude of the interchannel correlation, is proposed in [16] to detect earthquake-induced damage in DP SAR imagery collected over urbanized areas

$$r = \left| \langle i_{x,x} i_{x,y}^{*} \rangle \right| \tag{2}$$

where i stands for the complex SAR imagery, $\{x, y\} = \{V, H\}$ and $|\cdot|$ stands for modulus.

This metric is expected to exhibit lower values when measured over natural scenario; while larger values apply over areas that include man-made targets (e.g.; the urbanized area) since they call for large deviations from the reflection symmetry property. Damaged or collapsed building are expected to reduce the deviation from the reflection symmetry behavior resulting in r values closer to the ones that characterize natural scenarios. Hence, the bigger is the damage, the lower are the expected r values. This means that, assuming as a reference case the metric (2) evaluated using the pre-event imagery (r_{pre}), one can link the variability of r to the damage occurred in the built-up area according to the following feature:

$$\Delta r = r_{\text{pre}} - r_{\text{post}}. \tag{3}$$

Low Δr values (theoretically $\Delta r = 0$) are expected over urbanized areas not affected by the earthquake; while deviations from $\Delta r = 0$ are expected to correlate with increasing levels of damage.

The second DP metric is based on the methodology proposed in [17] and [26], which consists of analyzing the "change matrix" $\mathbf{C}_{\text{CD}}$ that is defined as follows:

$$\mathbf{C}_{\text{CD}} = \mathbf{C}_2 - \mathbf{C}_1 \tag{4}$$

where $\mathbf{C}_1$ and $\mathbf{C}_2$ are the covariance matrices which, obtained using a 5×5 average moving window, refer to two DP SAR acquisitions collected with the same geometry over the same scene but at two different times (before and after the earthquake).

The power difference between C_1 and C_2 can be maximized by solving the following eigenvalue problem [17]:

$$\mathbf{C}_{\text{CD}} \underline{\omega} = \lambda_i \underline{\omega} \tag{5}$$

with λ_i being the ith eigenvalue. Note that, since $\mathbf{C}_{\text{CD}}$ is no longer Hermitian and positive definite (HPSD), the eigenvalues can be also negative. Hence, the following metric is considered to detect earthquake-affected urbanized area [17]:

$$\lambda = \frac{1}{2} \sum_{i=1}^{2} |\lambda_i| . \tag{6}$$

In this study, the metric (6) is used to detect the levels of damage in DP SAR imagery. Low λ values (theoretically $\lambda = 0$) are expected over urbanized areas unaffected by the earthquake; while larger λ values are expected to correlate with stronger damage.

B. Damage Classification

The output of the two change detection metrics need to be linked to the discretized levels of damage. In this study, the image segmentation fast fuzzy c-means clustering (FFCM) is used to convert the changes observed by the metrics into levels of damage. Fuzzy c-means clustering (FCM) is one of the most popular image segmentation algorithms that allows one piece of data to be assigned to two or more clusters. This method, developed in [27] and improved in [28], is based on minimization of the following objective function:

$$J_m = \sum_{i=1}^{N} \sum_{i=1}^{C} u_{ij}^{m} \left\| x_i - c_j \right\|^2, \ 1 \le m < \infty \tag{7}$$

where $m > 1$ is a constant that controls the degree of fuzziness, u_{ij} is the degree of membership of x_i in the cluster j, x_i is the grey-level value of the ith pixel of the interest image, c_j is the centroid of the jth cluster, and $\|\cdot\|$ is the norm. The membership function u_{ij} represents the probability of a pixel belonging to a specific cluster, which depends on the distance between the pixel and each cluster center. To partition the image, an iterative optimization of the objective function (7) is performed, which consists of updating the membership function u_{ij}:

$$u_{ij} = \frac{1}{\sum_{k=1}^{C} \left(\frac{\|x_i - c_j\|}{\|x_i - c_k\|} \right)^{\frac{2}{m-1}}} \tag{8}$$

where

$$c_j = \frac{\sum_{i=1}^{N} u_{ij}^{m} x_i}{\sum_{i=1}^{N} u_{ij}^{m}} \tag{9}$$

is the cluster center. The iteration stops when

$$\max_{ij} \left\{ \left| u_{ij}^{(k+1)} - u_{ij}^{(k)} \right| \right\} < \varepsilon \tag{10}$$

where ε is a termination criterion whose values that range between 0 and 1, whereas k is the iteration step.

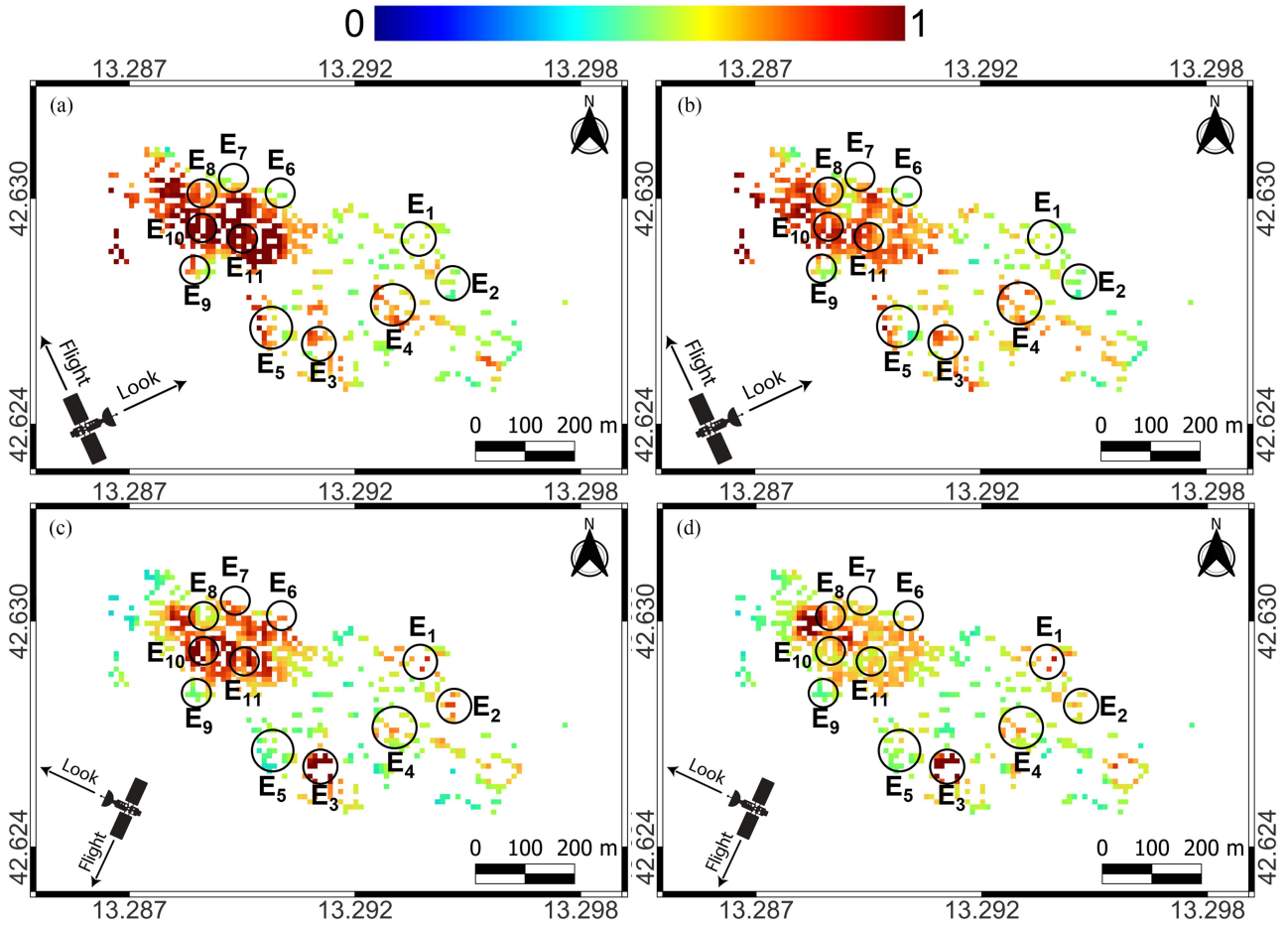

Fig. 3. Excerpt of the total scattering power (SPAN) related to the Sentinel-1 SAR imagery collected over the area of Amatrice, Italy under ascending and descending passes (first and second row, respectively), and before and after the earthquake (first and second column, respectively).

FCM results to be very expensive to converge in terms of computational time. Hence, an improved FCM version is used, namely FFCM, which consists of decreasing the number of distance calculations by checking the membership value for each point and eliminating those points with a membership value smaller than a threshold value.

C. Combination of Ascending and Descending Orbits

In this section, the combination of the DP processing outputs obtained from ascending and descending datasets is discussed. Two simple approaches are presented that combine the outputs of the features before and after the FFCM partitioning in a straightforward way.

The first combination (see Fig. 2) consists of summing up the DP features evaluated using ascending and descending datasets

$$x_{ad} = x_a + x_d \tag{11}$$

where x_a and x_d (with $x = \{\Delta r, \lambda\}$) are related to the DP feature outputs obtained from ascending and descending orbits, respectively. Then, the damage map $U_{x_{ad}}$ is obtained by applying the FFCM classifier to the output of equation (11).

The second combination (see Fig. 2) consists of the arithmetical mean between outputs of the FFCM classifier

$$\bar{U}_{x_{ad}} = \frac{U_{x_a} + U_{x_d}}{2} \tag{12}$$

where U_{x_a} and U_{x_d} are the output of the FFCM for ascending and descending orbits, i.e., the average of the two classified maps. Note that $\bar{U}_{x_{ad}}$ is rounded to the nearest integers toward infinity.

IV. Experiment

In this section, first, the sensitivity of the backscatter to the orbiting passes is discussed; then the PolSAR damage detection features are show for both the ascending and descending orbits and their sensitivity to damaged areas is discussed. Finally, the damage maps estimated combining ascending and descending passes are discussed against ground survey information.

A. Sensitivity of the Total Backscatter to the Orbiting Passes

The squared-modulus associated to the co- and cross-polarized channels, i.e., the SPAN, is displayed in the ascending [first row (a-b)] and descending [second row (c-d)] cases and both before [first column (a–c)] and after [second column

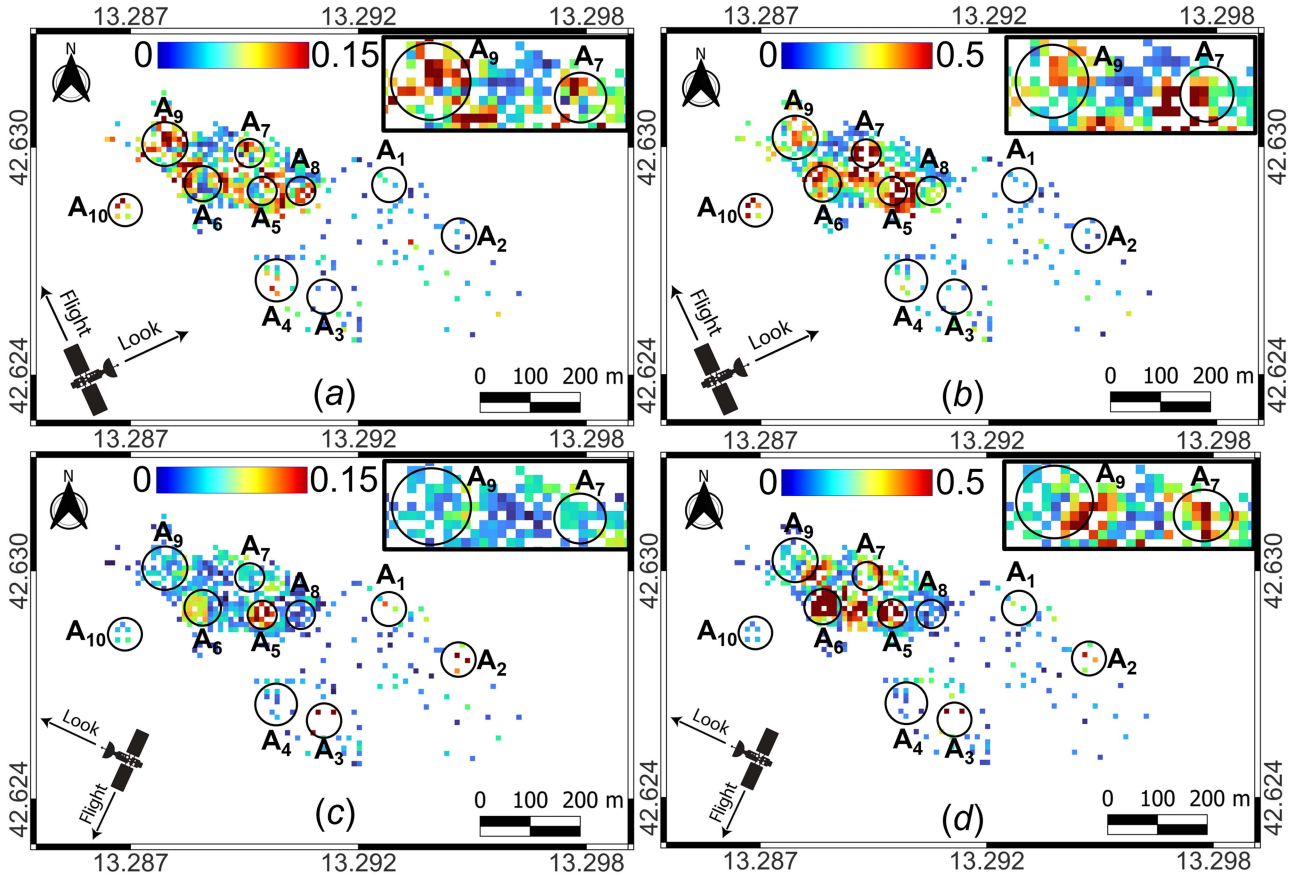

Fig. 4. Polarimetric features evaluated over the area of Amatrice. The figure is organized in a matrix format: the first and the second rows stand for SAR imagery collected in ascending and descending mode, respectively. The first and the second columns refer to Δr and λ, respectively. (a) Δr_a; (b) λ_a; (c) Δr_d; (d) λ_d.

(b-d)] seismic event in Fig. 3. Note that the area out of the city of Amatrice is masked out using the building footprint extracted from OpenStreetMap (OSM). The SPAN imagery clearly show that the upper-left part of the city area results in the largest backscattering, since it is the area calling for the highest urbanization. The center- and the rightmost part of the image call for a lower backscattering since buildings are very spread with vegetated areas. This behavior applies for both ascending and descending passes (a–c). As expected, after the earthquake event, the radar backscattering reduces and the decreasing rate is more pronounced in the more densely urbanized area (i.e., the upper-left part of the image). There is also a remarkable sensitivity of the SPAN to the orbiting passes. The scene collected in ascending pass exhibits an overall backscatter larger than the descending one both in the pre- and in the postevent cases. It can also be noted that the south-eastern part of the city, which calls for a lower level of urbanization, does not show significant differences in SAR response between ascending and descending passes. All this matter suggests a joint exploitation of polarization diversity and orbiting passes to improve the estimation of damage levels. Note that a different incidence angle applies for the ascending and descending cases that also plays a role. To better investigate complementarities and similarities in the total backscatering behavior under ascending and descending passes, region of interests (ROIs) are selected in the imagery of Fig. 3. The ROIs labeled as E_1–E_5, which belong to the city area resulting in a lower level of urbanization, call for a complementary scattering behavior when observed in the scenes collected under ascending and descending passes. The ROIs labeled as E_1–E_3 call for the largest backscattering under descending pass. The opposite behavior is achieved within the regions labeled as E_4–E_5, where the largest backscattering is obtained in the ascending case. The ROIs E_6–E_{11}, which belong to the area calling for the highest level of urbanization, are such that E_6–E_7 (E_8–E_9) call for the largest backscattering in the descending (ascending) passes. Similarities also applies between the backscatter resulting from scenes collected under ascending and descending passes. Most of these similarities are present in the rural areas, and remarkable cases can be identified in the highly urbanized area, such as in E_{10} and E_{11}. This analysis points out that the combination of scenes collected under ascending and descending passes is informative especially in the densely urbanized area since it contributes to better catch scattering details associated to blocks of buildings.

B. *Sensitivity to PoLSAR Metrics to Damaged Areas*

PolSAR change detection features are displayed in Fig. 4, where the two columns stand for Δr (3) and λ (6), respectively; while the two rows stand for features evaluated using the ascending and descending metrics, respectively. The area out of the city of Amatrice is again masked out using the ground information

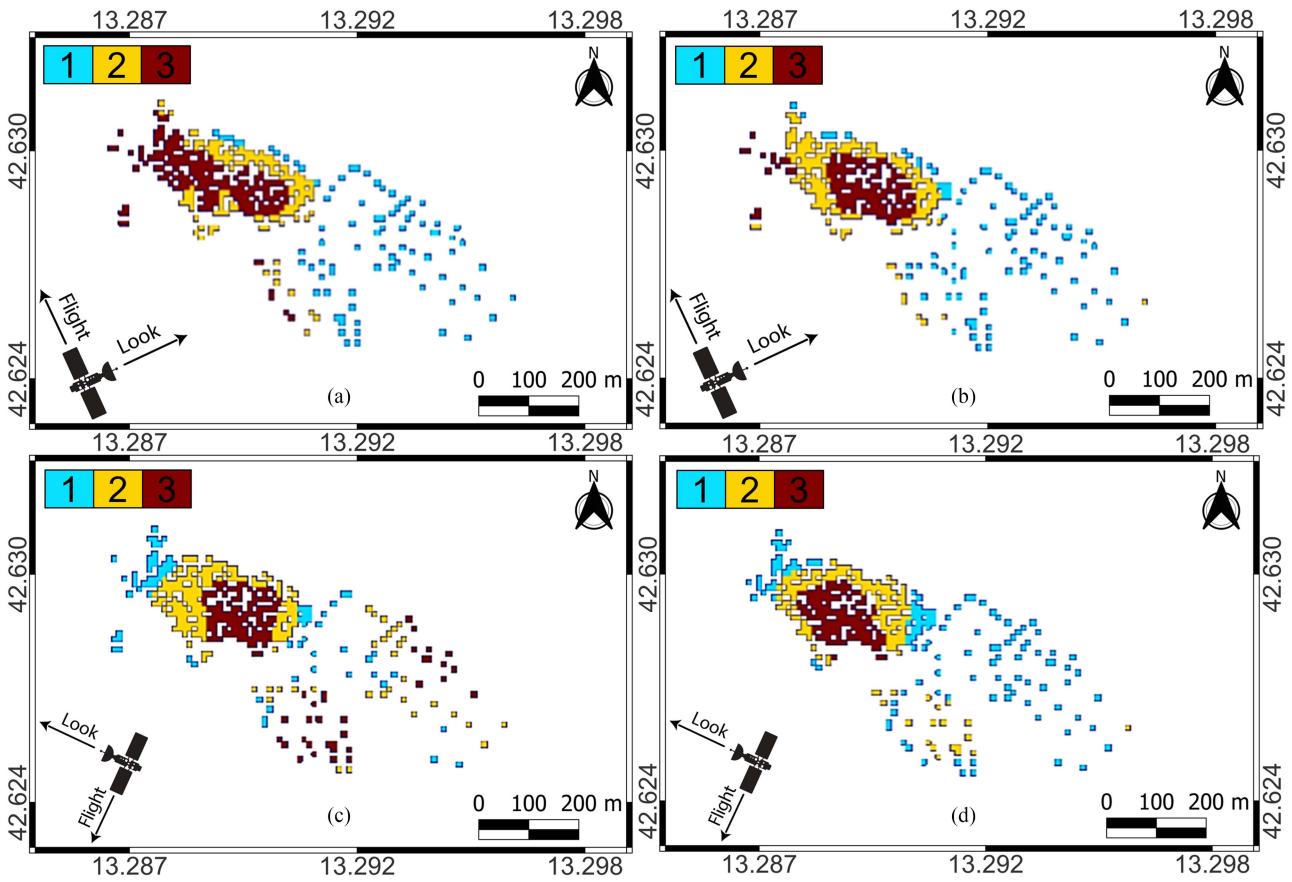

Fig. 5. FFCM classification output evaluated over the polarimetric outputs of Fig. 4. The figure is organized in matrix format: the first and the second rows stand for SAR imagery collected in ascending and descending mode, respectively. The first and the second columns refer to polarimetric feature Δr and λ, respectively: (a) $U_{\Delta r_a}$; (b) U_{λ_a}; (c) $U_{\Delta r_d}$; (d) U_{λ_d}.

of Fig. 1. The images show that the two metrics, both in the ascending and the descending cases, result in the largest changes in the upper-left part of Amatrice. This agrees with the ground information of Fig. 1. Moreover, the two metrics show a different sensitivity according to the orbiting pass. The largest difference between the two metrics is achieved in the descending pass, see Fig. 4(c) and (d). In fact, λ_d reveals changes larger than Δr_d in the highest urbanized part of the city. It must be however noted that, since the two metrics span completely different range of values, the different sensitivity does not necessarily will result in different detected class of damages.

Even in this case, to better investigate complementarities and similarities in the change detection PolSAR features, ROIs are selected in the imagery of Fig. 4. The ROIs labeled as A_1–A_4, which belong to the city area resulting in a lower level of urbanization, call for a complementary behavior when observed in the scenes collected under ascending and descending passes. The ROIs labeled as A_1–A_3 call for the largest changes under descending pass. The opposite behavior is achieved within the region labeled as A_4 where the largest changes are obtained in the ascending case. The ROIs A_5–A_{10}, which belong to the area calling for the highest level of urbanization, are such that A_5–A_6 (A_7–A_{10}) call for the largest changes in the descending (ascending) passes. To better visually inspect changes that occurred in the two metrics in both ascending and descending passes, an enlarged version of the area that includes the ROIs A_7 and A_9 is annotated in Δr_d [see Fig. 4(c)]. However, it must be explicitly noted that those changes are non-negligible and they can be hardly compared with λ_d [see Fig. 4(d)], since Δr and λ call for different ranges of values. By contrasting the outputs each metric under the two passes [see Fig. 4(a)–(c) and Fig. 4(b)–(d)] it can be noted that Δr exhibits the largest sensitivity to the orbiting pass.

C. Damage Classification and Ascending/Descending Orbits Combination

In this section, experimental results obtained processing the SAR dataset augmented with auxiliary external ground information are discussed. First, the levels of damage are quantified using an unsupervised classifier based on the FFCM applied to the whole SAR scene. Then, the damage maps obtained from ascending and descending orbits are properly combined using (11) and (12). Finally, to analyze the accuracy of the estimated levels of damage, the ground information map [see Fig. 1(b)] is used.

The first experiment consists of generating the range maps using the FFCM that is applied separately to the ascending and descending orbits. The FFCM outputs are depicted in Fig. 5, where 3 levels of damage have been selected, according to the

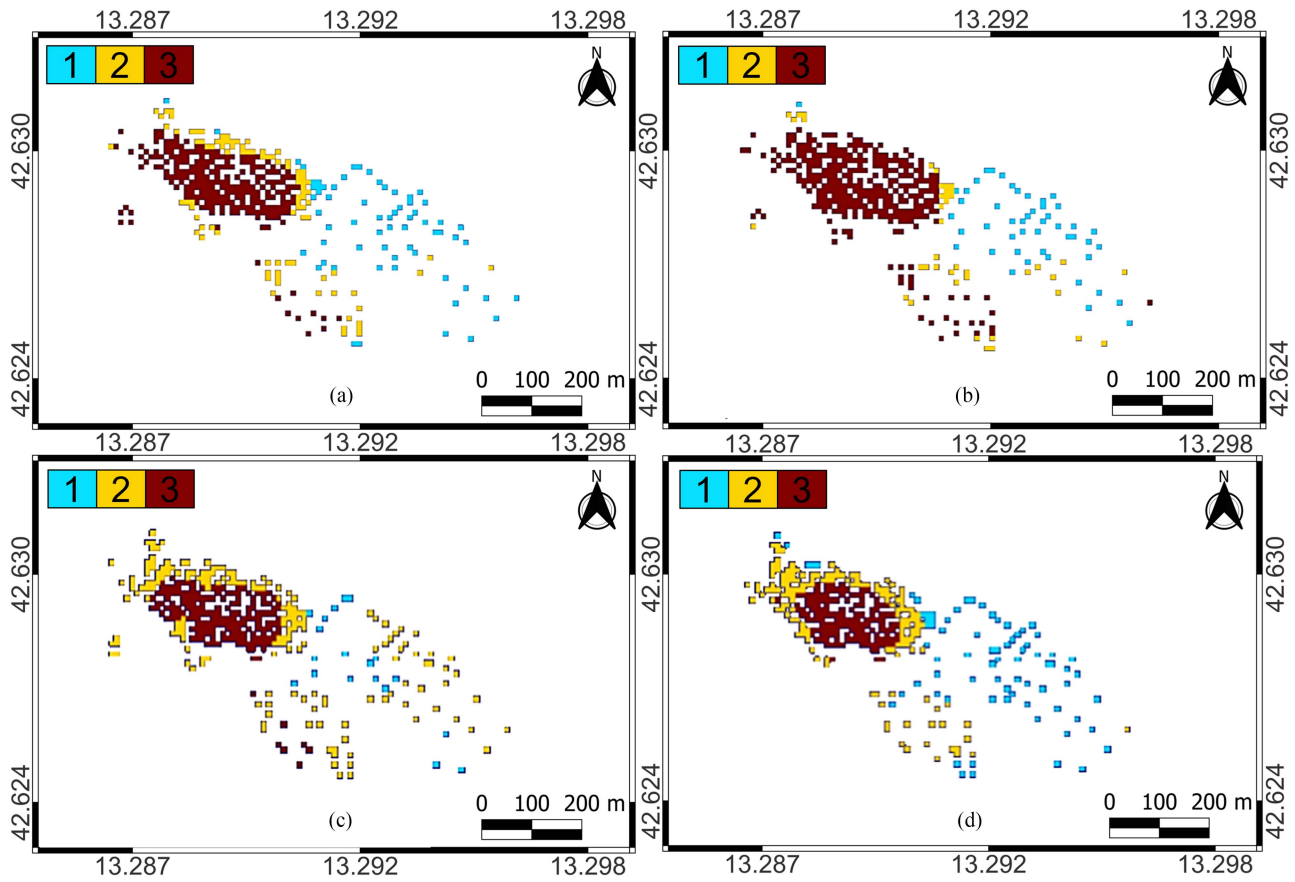

Fig. 6. FFCM classification output evaluated over the polarimetric outputs of Fig. 4. The figure is organized in matrix format: the first and the second rows stand for the outputs of equation (11) and (12), respectively. The first and the second columns refer to polarimetric feature Δr and λ, respectively: (a) $U_{\Delta r_{ad}}$; (b) $U_{\lambda_{ad}}$; (c) $\bar{U}_{\Delta r_{ad}}$; (d) $\bar{U}_{\lambda_{ad}}$.

TABLE II
CONFUSION MATRIX BETWEEN THE SAR-BASED ESTIMATIONS AND THE FILTERED GROUND INFORMATION EVALUATED OVER THE CITY OF AMATRICE, WHERE 1, 2, AND 3 STAND FOR LOW, MEDIUM, AND HIGH DAMAGE

	UA (%)			PA (%)			OA (%)	K (%)
Feature	1	2	3	1	2	3		
$U_{\Delta r_a}$	76.5	7.7	56.5	16.1	4.1	93.6	49.2	9.6
$U_{\Delta r_d}$	0	41.7	34.8	0	14.5	77.1	34.2	3.6
$U_{\Delta r_{ad}}$	21.1	16.1	71.9	6.4	10.1	94.3	63.7	16.4
$\bar{U}_{\Delta r_{ad}}$	0	76.3	58.6	0	25.7	96.2	58.7	23.1
U_{λ_a}	88.2	13.9	43.7	16.5	5.6	97.1	40.6	7.4
U_{λ_d}	47.4	17	38.7	7.2	7	100	35.8	5.77
$\boldsymbol{U_{\lambda_{ad}}}$	**15.8**	**25.4**	**92**	**7.1**	**41**	**91.8**	**77.8**	**36.2**
$\bar{U}_{\lambda_{ad}}$	41.2	22.4	49.8	9.9	8.4	100	45.2	10

ground truth presented in Section II. By visually inspecting the images produced by FFCM, differences can be observed both in the outputs of the features (see Δr and λ images in the first and second column of Fig. 5, respectively). As suggested by the previous sensitivity analysis, Δr results in the largest sensitivity to the orbiting pass resulting in different damage levels in both the urbanized and the rural areas of Amatrice according to the orbiting pass selected. The Δr map related to the ascending pass [see Fig. 5(a) results in a damage level 3 that is quite spread in the urbanized area and practically absent in the rural area that mostly calls for damage level 1. When dealing with the Δr map obtained processing the descending pass (Fig. 5(c))] the damage level 3 is quite narrow in the urbanized area and the rural area is mostly dominated by damage of level 2 and 3. The λ maps obtained under ascending and descending passes [see Fig. 5(b) and (d), respectively] only show slightly changes in terms of damage levels. It can be also noted that in some areas the features, which in Fig. 4 result in a different sensitivity to the orbiting passes, call for the same damage class. This is not surprising since the FFCM is separately applied to the two orbits.

To quantitatively analyze the performance of the detection methods, the ground information of Fig. 1 is used. Note that the latter is smoothed using a $N \times N$ average moving window, with $N = 15$ to cope with the different spatial scales that result for the SAR-derived maps (that contain information on aggregated blocks of buildings) and the point-wise ground truth. Note that $N = 15$ is chosen since it gives the best result in terms of overall accuracy with the SAR-derived maps. The quantitative analysis consists of calculating the confusion matrix whose synthetic parameters are: overall accuracy (OA), user accuracy (UA), producer accuracy (PA), and kappa coefficient (K) [29]. OA measures how all the reference classes are correctly mapped; UA is the probability that a value predicted to be in a certain class really belongs to that class, i.e., it is the ratio of correctly predicted values to the total number of values predicted to be in

that class. PA is the probability that a value in a given class is correctly classified, i.e., the ratio of correctly predicted elements to the total (true) number of elements in that class, and the *K* coefficient provides an overall analysis of the classification performance with respect to a reference random classifier.

The parameters listed in Table II quantitatively confirm that Δr results in the largest sensitivity to the orbiting passes and they also point out that the descending pass calls for an accuracy worse than the ascending one for both the features. It can be also noted that Δr is not able to detect "level 1" damage under the descending pass. The third class of damage is well-identified by both the metrics and both the ascending and descending passes. To summarize, Δr performs better than λ when the scenes collected under the ascending pass are used; while the performance of λ is slightly better than the Δr one under the descending pass.

The second experiment is to discuss the accuracy of the damage maps obtained by jointly exploiting ascending and descending passes. The FFCM outputs are depicted in Fig. 6, where the two rows refer to $U_{x_{ad}}$ (11) and $\bar{U}_{x_{ad}}$ (12), respectively; while columns stand for Δr and λ metrics, respectively. By visually inspecting the damage maps one can note a remarkable sensitivity of the detected damage levels to both the feature and the orbiting pass. A visual comparison of the detected map with the filtered ground information of Fig. 1(b) shows that the approach (11) results in the best performance for both the features although misclassifications appear in both the very left-hand-side of the image and in the central part, i.e., areas that are nondensely urbanized. The feature λ appears to provide the best performance especially in the densely urbanized area. To quantitatively discuss the estimation accuracy, the confusion matrix is evaluated by contrasting pixel-by-pixel the map of Fig. 6 with the ground truth map of Fig. 1(b). The output parameters of the confusion matrix (listed in Table II) show a non-negligible improvement in terms of OA. With respect to the Δr feature, the OA reaches up to $\sim 64\%$ (i.e., $+\sim 15\%$ with respect to the use of the single orbiting pass) when the first approach is used (11) to combine the orbiting passes. When the combination is performed according to (12), the OA degrades down to $\sim 59\%$ witnessing that the combination of the DP feature's outputs performs better than the combination of FFCM outputs. With respect to the λ feature, the OA reaches up to $\sim 78\%$ (i.e., $+\sim 37\%$ with respect to the use of the single orbiting pass) when the approach (11) is used. Again, the combination of DP feature's outputs performs better than the combination of FFCM outputs with the latter resulting in a OA that decrease down to $-\sim 45\%$. In summary, we can state that the combination performed by (11) is always better than the FFCM output combination. As far as the accuracy performance, based on the ground truth data collection, it is worth noting that the in situ survey is not free from errors. Pierdicca et al. [30] showed that reference data (i.e., the ground truth) cannot be completely reliable. By adopting the triple collocation technique, they compared damage classification with two different ground surveys for the L'Aquila 2009 earthquake. They found that the satellite product, in that case study derived by VHR optical data, can have accuracy comparable to that of one ground surveys versus the other ground surveys, especially in terms of omission and commission errors, that are about 0.5. Therefore, if we consider the worst resolution of SAR data, the possible inaccuracy of the in situ survey, and - of course - the spatial filtering of the GT itself to match SAR features, we can easily understand the quite low accuracy of the proposed method.

V. Conclusion

In this study, the joint use of dual-polarization SAR measurements collected in ascending and descending orbit pass is exploited to quantify post damage of the Central Italy earthquake that occurred in 2016. First, a processing chain that consists of using DP SAR features to be ingested in an unsupervised Fuzzy c-means classifier, is introduced to quantify the levels of damage. Then, the ascending and descending damage maps are properly combined and the estimated damage maps are contrasted with the ground information. Experimental results, obtained using C–band Sentinel–1 SAR imagery collected over the city of Amatrice in Lazio (Italy) in ascending and descending pass, confirm the soundness of the proposed approach, showing that the joint use of ascending and descending orbits allows improving the results in terms of overall accuracy. In details:

1) The joint use of ascending/descending passes always improve the OA with respect to the single orbiting pass.
2) The two features exhibit different sensitivity to the damage according to the processed orbiting pass.
3) The λ feature outperforms Δr when the two passes are combined.
4) The combination of the orbiting passes performed on the feature's outputs [i.e. eq. (11)] outperforms the combination performed using FFCM outputs [i.e., (12)].
5) The main improvement is obtained over densely urbanized areas.

Even though different orbit data fusion increases the accuracy of damage classification with respect to single pass approaches, some studies need to be performed in the future, in order to find a more suitable integration method, with the purpose to exploit also the information about the urban texture that plays an important role as revealed by our work.

References

[1] S. Stramondo, C. Bignami, M. Chini, N. Pierdicca, and A. Tertulliani, "Satellite radar and optical remote sensing for earthquake damage detection: Results from different case studies," *Int. J. Remote Sens.*, vol. 27, no. 20, pp. 4433–4447, 2006.

[2] L. Gong, C. Wang, F. Wu, J. Zhang, H. Zhang, and Q. Li, "Earthquake-induced building damage detection with post-event sub-meter VHR TerraSAR-X staring spotlight imagery," *Remote Sens.*, vol. 8, no. 11, pp. 887–908, 2016.

[3] C. Yonezawa and S. Takeuchi, "Decorrelation of SAR data by urban damages caused by the 1995 Hyogoken-Nanbu earthquake," *Int. J. Remote Sens.*, vol. 22, no. 8, pp. 1585–1600, 2001.

[4] E. J. M. Rignot and J. J. van Zyl, "Change detection techniques for ERS-1 SAR data," *IEEE Trans. Geosci. Remote Sens.*, vol. 31, no. 4, pp. 896–906, Jul. 1993.

[5] M. Matsuoka and F. Yamazaki, "Use of satellite SAR intensity imagery for detecting building areas damaged due to earthquakes," *Earthq. Spectra*, vol. 20, no. 3, pp. 975–994, 2004.

[6] P. Gamba, F. Dell'Acqua, and G. Lisini, "Change detection of multitemporal SAR data in urban areas combining feature-based and pixel-based techniques," *IEEE Trans. Geosci. Remote Sens.*, vol. 44, no. 10, pp. 2820–2827, Oct. 2006.

[7] V. Romaniello, A. Piscini, C. Bignami, R. Anniballe, and S. Stramondo, "Earthquake damage mapping by using remotely sensed data: The Haiti case study," *J. Appl. Remote Sens.*, vol. 11, no. 1, pp. 1–16, 2017.

[8] D. Brunner, G. Lemoine, and L. Bruzzone, "Earthquake damage assessment of buildings using VHR optical and SAR imagery," *IEEE Trans. Geosci. Remote Sens.*, vol. 48, no. 5, pp. 2403–2420, May 2010.

[9] P. Uprety, F. Yamazaki, and F. Dell'Acqua, "Damage detection using high-resolution SAR imagery in the 2009 l'aquila, Italy, earthquake," *Earthq. Spectra*, vol. 29, no. 4, pp. 1521–1535, 2013.

[10] M. Watanabe, T. Motohka, Y. Miyagi, C. Yonezawa, and M. Shimada, "Analysis of urban areas affected by the 2011 off the pacific coast of tohoku earthquake and tsunami with L-band SAR full-polarimetric mode," *IEEE Geosci. Remote. Sens. Lett.*, vol. 9, no. 3, pp. 472–476, May 2012.

[11] S. W. Chen, X. S. Wang, and S. P. Xiao, "Urban damage level mapping based on co-polarization coherence pattern using multitemporal polarimetric SAR data," *IEEE J. Sel. Topics Appl. Earth Observ. Remote Sens.*, vol. 11, no. 8, pp. 2657–2667, Aug. 2018.

[12] F. Nunziata, M. Migliaccio, and X. Li, "Sea oil slick observation using hybrid-polarity SAR architecture," *IEEE J. Ocean. Eng.*, vol. 40, no. 2, pp. 426–440, Apr. 2015.

[13] A. Buono, F. Nunziata, M. Migliaccio, and X. Li, "Polarimetric analysis of compact-polarimetry SAR architectures for sea oil slick observation," *IEEE Trans. Geosci. Remote Sens.*, vol. 54, no. 10, pp. 5862–5874, Oct. 2016.

[14] M. Watanabe et al., "Detection of damaged urban areas using interferometric SAR coherence change with PALSAR-2," *Earth Planets Space*, vol. 68, no. 1, pp. 1–12, Jul. 2016.

[15] S. Karimzadeh and M. Mastuoka, "Building damage assessment using multisensor dual-polarized synthetic aperture radar data for the 2016 m 6.2 Amatrice earthquake, Italy," *Remote Sens.*, vol. 9, no. 4, pp. 1–17, 2017.

[16] E. Ferrentino, F. Nunziata, M. Migliaccio, and A. Vicari, "A sensitivity analysis of dual-polarization features to damage due to the 2016 central-Italy earthquake," *Int. J. Remote Sens.*, vol. 39, no. 20, pp. 6846–6863, 2018.

[17] E. Ferrentino, A. Marino, F. Nunziata, and M. Migliaccio, "A dual–polarimetric approach to earthquake damage assessment," *Int. J. Remote Sens.*, vol. 40, no. 1, pp. 197–217, 2019.

[18] E. Ferrentino, F. Nunziata, C. Bignami, L. Graziani, A. Maramai, and M. Migliaccio, "Multi-polarization c-band sar imagery to quantify damage levels due to the central Italy earthquake," *Int. J. Remote Sens.*, vol. 42, no. 15, pp. 5969–5984, 2021.

[19] T. Lillesand, R. Kiefer, and J. Chipman, *Remote Sensing and Image Interpretation*. Hoboken, NJ, USA: Wiley, 2004.

[20] S. Karimzadeh and M. Matsuoka, "Building damage characterization for the 2016 amatrice earthquake using ascending–descending COSMO-skyMed data and topographic position index," *IEEE J. Sel. Topics Appl. Earth Observ. Remote Sens.*, vol. 11, no. 8, pp. 2668–2682, Aug. 2018.

[21] R. Azzaro et al., "The 24 Aug. 2016 Amatrice earthquake: Macroseismic survey in the damage area and EMS intensity assessment," *Ann. Geophys.*, vol. 59, pp. 1–18, 2016.

[22] L. Graziani, S. Mese, A. Tertulliani, L. Arcoraci, A. Maramai, and A. Rossi, "Investigation on damage progression during the 2016–2017 seismic sequence in Central Italy using the European Macroseismic Scale (EMS-98)," *Bull. Earthq. Eng.*, vol. 17, no. 10, pp. 5535–5558, May 2019.

[23] G. Grünthal, *Eur. Macroseismic Scale 1998 (EMS-98) European Seismological Commission*, Cahiers du Centre Européen de Géodynamique et de Séismologie, vol. 15, Luxembourg, 1998.

[24] S. Cloude, *Polarisation: Applications in Remote Sensing*. Oxford, U.K.: OUP Oxford, 2009.

[25] F. Nunziata, M. Migliaccio, and C. E. Brown, "Reflection symmetry for polarimetric observation of man-made metallic targets at sea," *IEEE J. Ocean. Eng.*, vol. 37, no. 3, pp. 384–394, Jul. 2012.

[26] A. Marino and M. Nannini, "Signal models for changes in polarimetric SAR data," *IEEE Trans. Geosci. Remote Sens.*, vol. 60, pp. 1–18, 2022.

[27] J. C. Dunn, "A fuzzy relative of the isodata process and its use in detecting compact well-separated clusters," *J. Cybern.*, vol. 3, no. 3, pp. 32–57, 1973.

[28] J. C. Bezdek, *Pattern Recognition With Fuzzy Objective Function Algorithms*. USA: Kluwer Academic, 1981.

[29] J. R. Jensen, *Introductory Digital Image Processing: A. Remote Sensing Perspective*, 4th ed. Upper Saddle River, NJ, USA: Prentice Hall Press, 2015.

[30] N. Pierdicca et al., "Triple collocation to assess classification accuracy without a ground truth in case of earthquake damage assessment," *IEEE Trans. Geosci. Remote Sens.*, vol. 56, no. 1, pp. 485–496, Jan. 2018.